PNAS
www.pnas.org

Supplementary Information for

High-frequency microrheology in 3D reveals mismatch between cytoskeletal and extracellular matrix mechanics

Jack R. Staunton, Woong Young So, Colin D. Paul and Kandice Tanner*

*Corresponding author: Dr. Kandice Tanner; Center for Cancer Research, National Cancer Institute, Building 37, Room 2132, Bethesda, MD 20892; Ph: 260-760-6882
Email: kandice.tanner@nih.gov

This PDF file includes:

Figs. S1 to S15
Supplementary method
Captions for movies S1 to S3

Other supplementary materials for this manuscript include the following:

Movies S1 to S3

www.pnas.org/cgi/doi/10.1073/pnas.1814271116

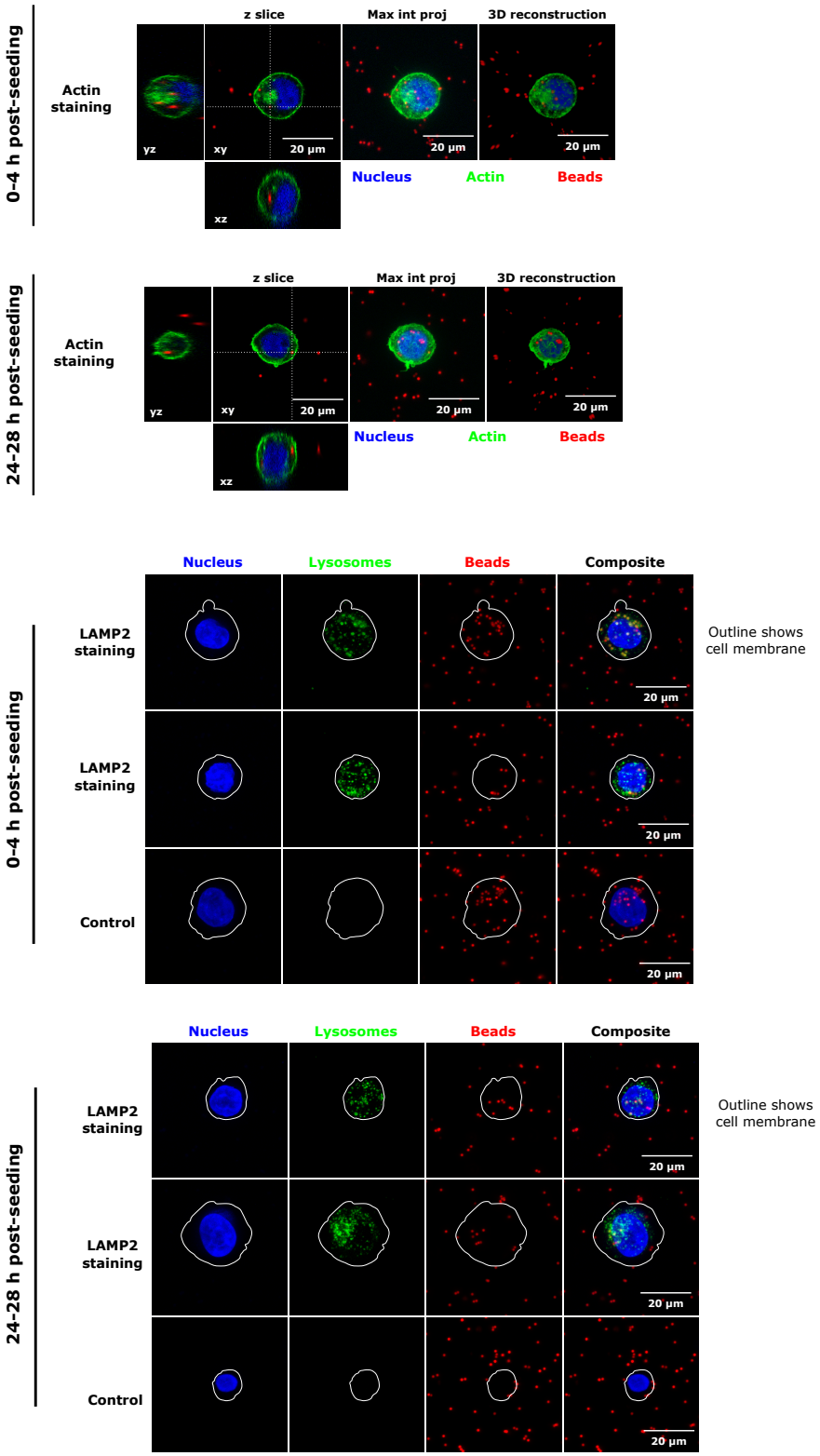

Fig. S1. Bead distributions inside embedded cells. Fluorescence confocal microscopy with staining for actin (phalloidin), nuclei (DAPI), and lysosomes (LAMP2).

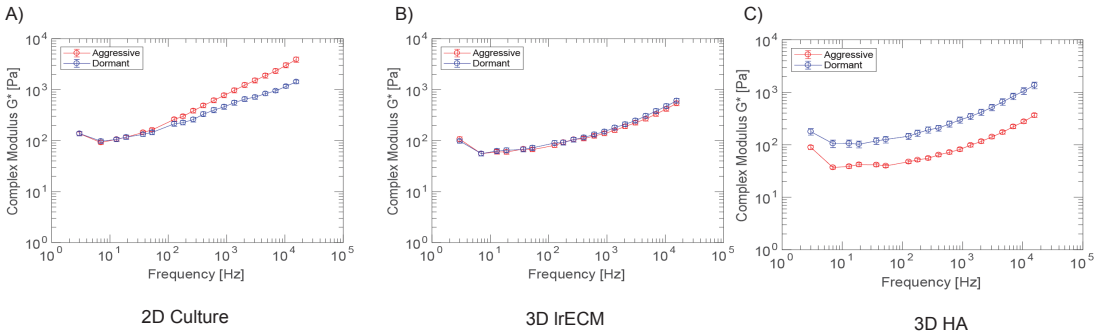

Fig. S2. Complex moduli of aggressive D2-A1 cells and dormant D2.0R cells in different microenvironments.

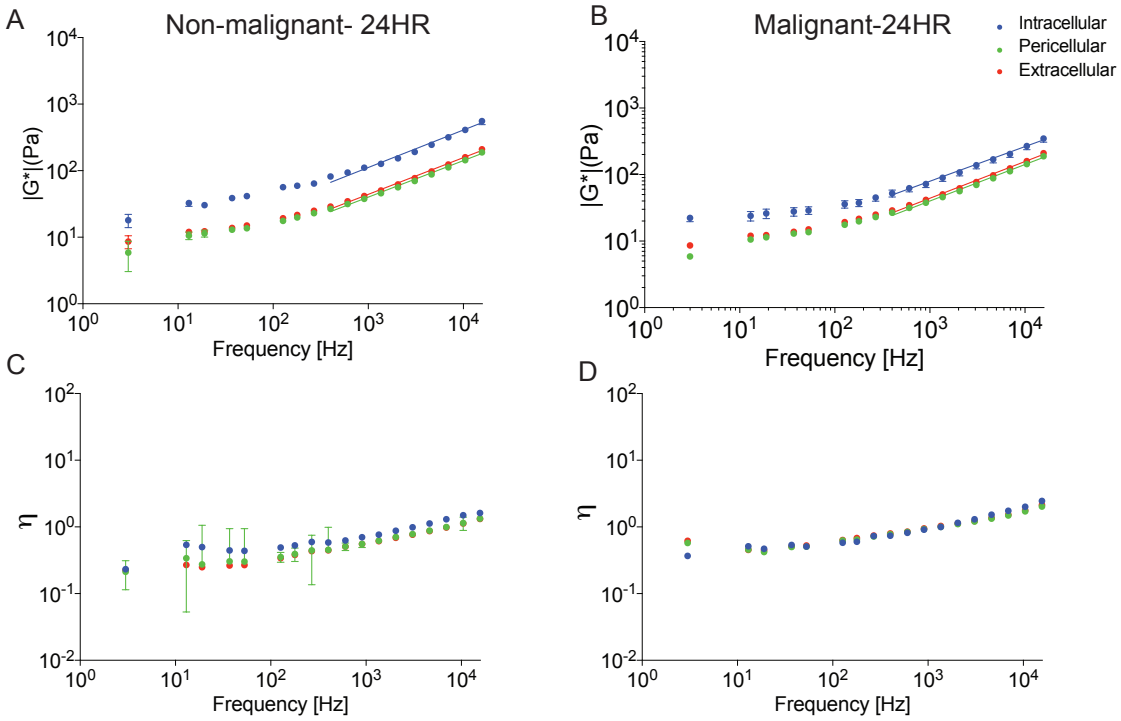

Fig. S3. Complex moduli and loss tangents of non-malignant MCF10A cells and malignant MCF10-CA1 cells after 24h incubation post-embedding.

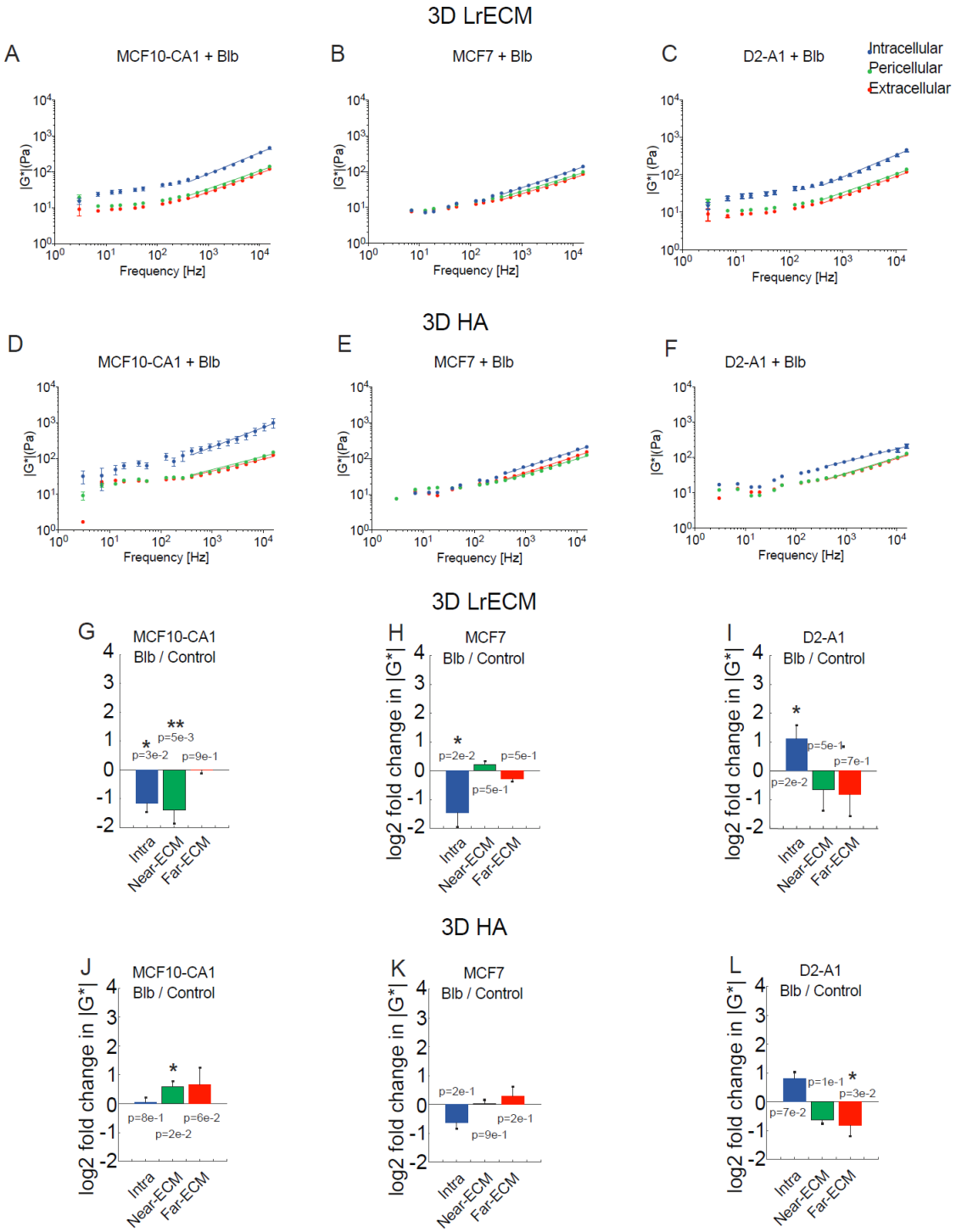

Fig. S4. Complex moduli of malignant MCF10-CA1 cells, non-tumorigenic MCF7 cells, and dormant D2-A1 cells embedded in lrECM and HA in presence of 10 µM blebbistatin. G-I) log2 ratios of blebbistatin-treated vs. untreated control $|G^*(\omega)|$ for MCF10-CA1 cells (G), MCF7 cells (H), and D2-A1 cells (I) embedded in 3D lrECM. J-L) log2 ratios of blebbistatin-treated vs. untreated control $|G^*(\omega)|$ for MCF10-CA1 cells (J), MCF7 cells (K), and D2-A1 cells (L) embedded in 3D HA. P-values from 2-way ANOVA are shown above or below each bar in G-L (* for $p<0.05$, ** for $p<0.01$, and *** for $p<0.001$).

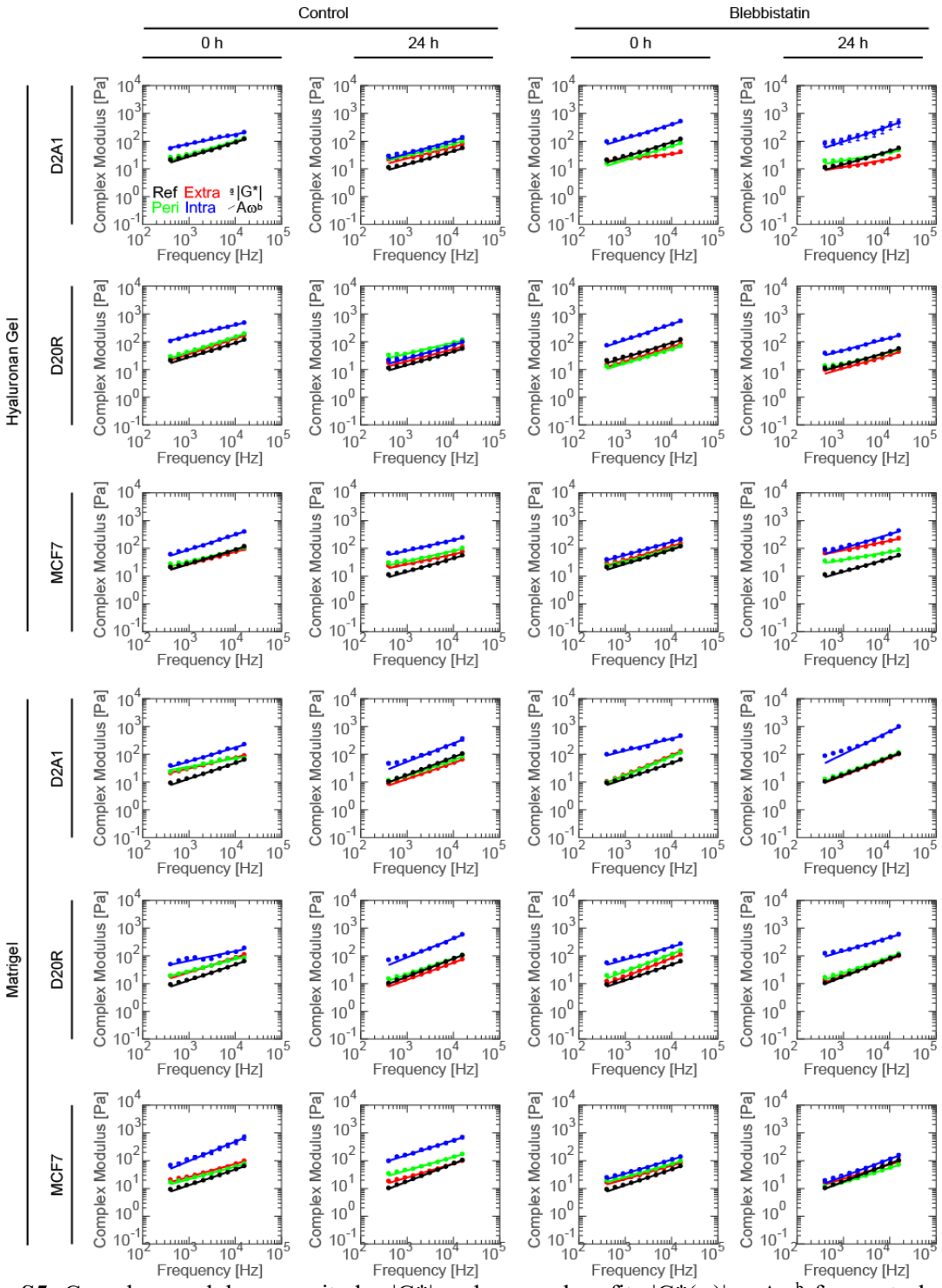

Fig. S5. Complex modulus magnitudes |G*| and power law fits $|G^*(\omega)| = A\omega^b$ for control and Blebbistatin. Mean complex modulus magnitudes |G*| vs. probe frequency for intracellular, pericellular (near-ECM) and extracellular (far-ECM) measurements of the indicated cell line, and that of the corresponding unoccupied reference gel. Lines of best fit to the power law $|G^*(\omega)| = A\omega^b$ for each condition are plotted in corresponding colors.

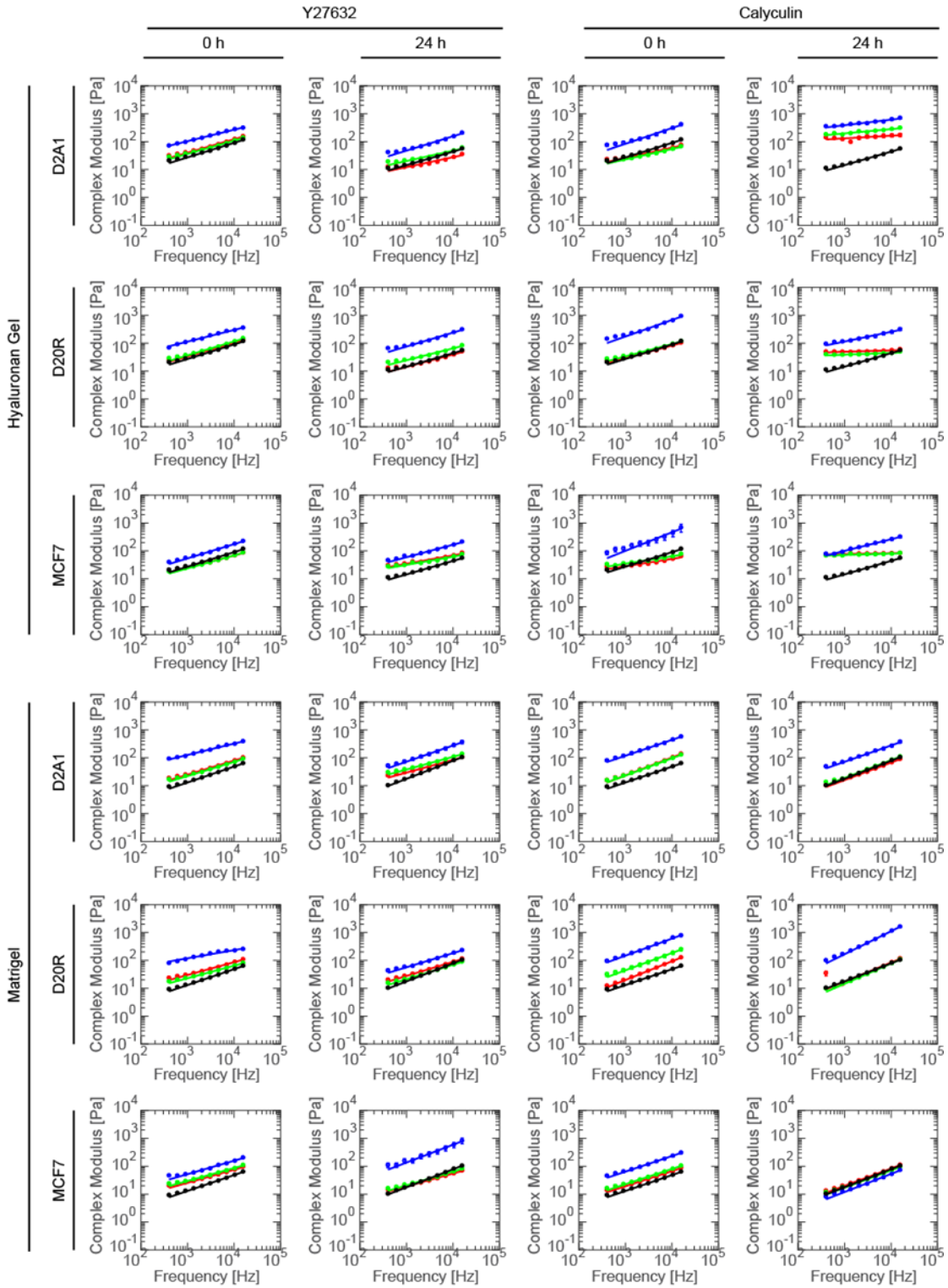

Fig. S6. Complex modulus magnitudes |G*| and power law fits $|G^*(\omega)| = A\omega^b$ for Y27632 and Calyculin A. Mean complex modulus magnitudes |G*| vs. probe frequency for intracellular, pericellular (near-ECM) and extracellular (far-ECM) measurements of the indicated cell line, and that of the corresponding unoccupied reference gel. Lines of best fit to the power law $|G^*(\omega)| = A\omega^b$ for each condition are plotted in corresponding colors.

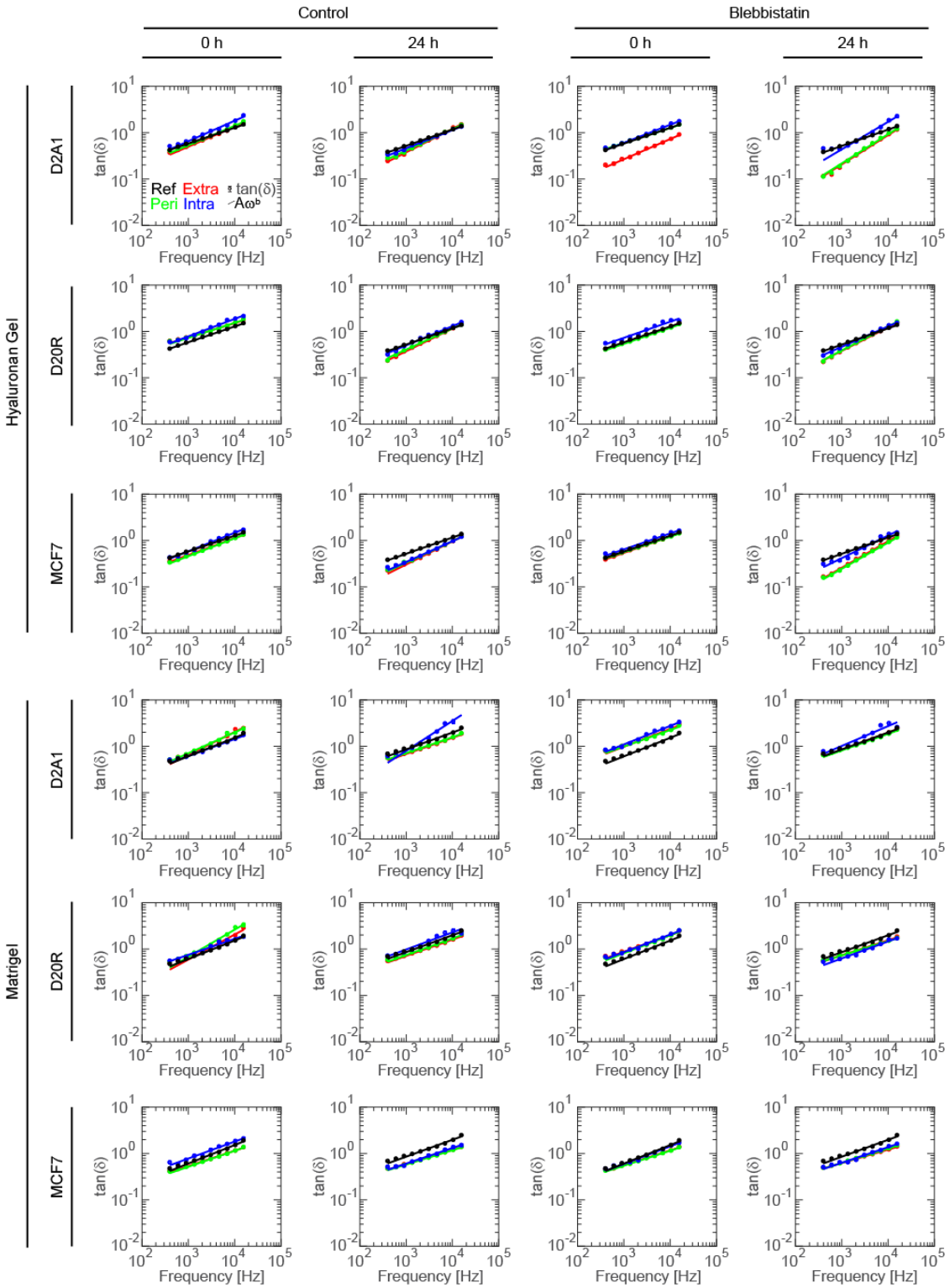

Fig. S7. Loss tangents tan(δ(ω)) and power law fits tan(δ(ω)) = $A\omega^b$ for control and Blebbistatin. Mean loss tangents tan(δ(ω)) vs. probe frequency for intracellular, pericellular (near-ECM) and extracellular (far-ECM) measurements of the indicated cell line, and that of the corresponding unoccupied reference gel. The line of best fit to the power law tan(δ(ω)) = $A\omega^b$ for each condition is plotted in the color corresponding to the data fit.

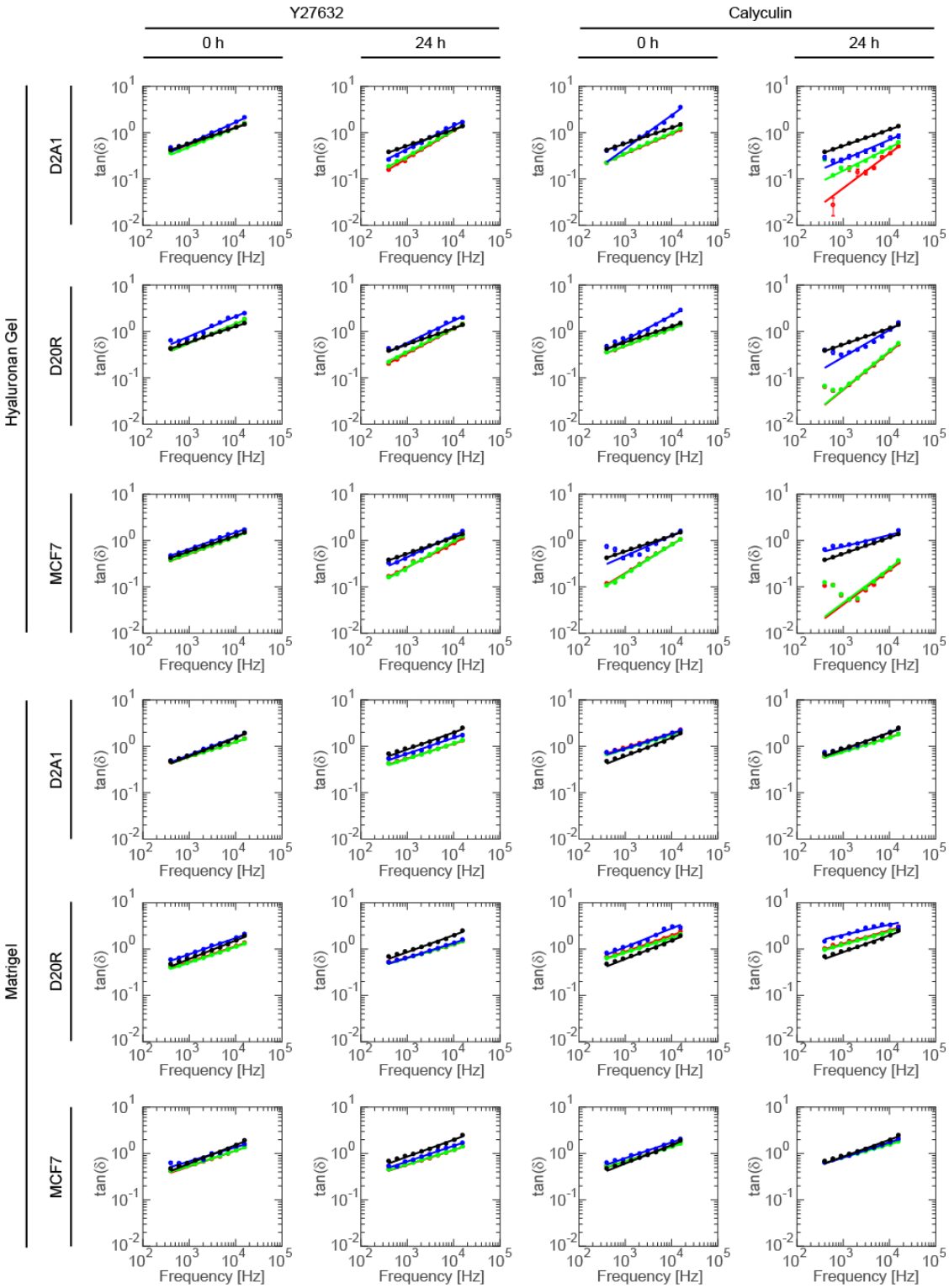

Fig. S8. Loss tangents tan(δ(ω)) and power law fits tan(δ(ω)) = $A\omega^b$ for Y27632 and Calyculin A. Mean loss tangents tan(δ(ω)) vs. probe frequency for intracellular, pericellular (near-ECM) and extracellular (far-ECM) measurements of the indicated cell line, and that of the corresponding unoccupied reference gel. The line of best fit to the power law tan(δ(ω)) = $A\omega^b$ for each condition is plotted in the color corresponding to the data fit.

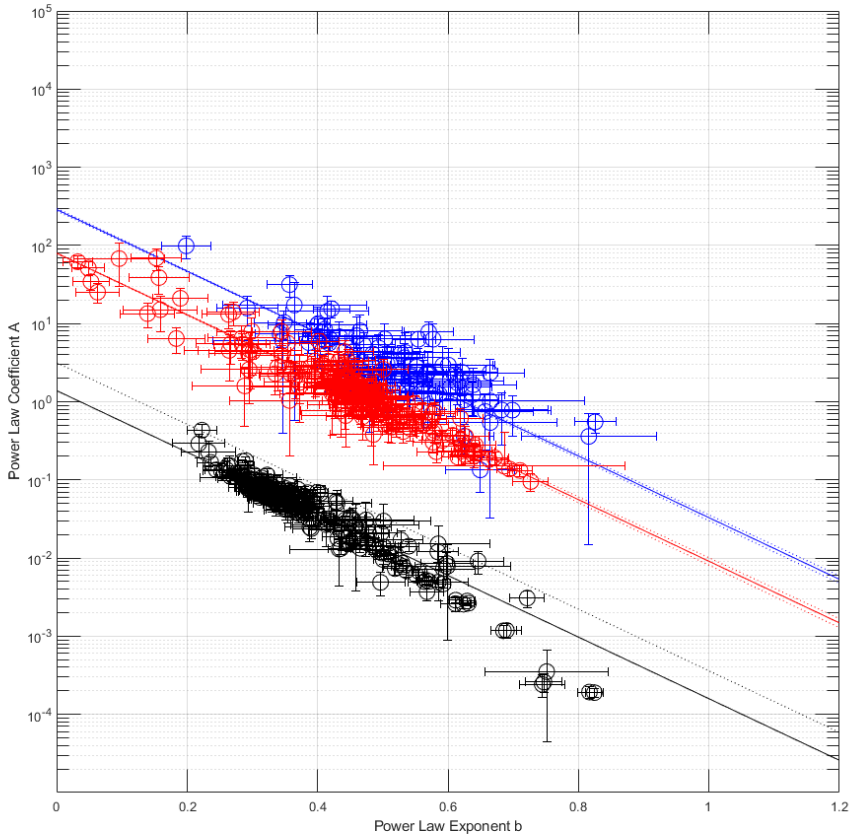

Fig. S9. Hysteresivity master curve plotted with intracellular and extracellular (near-ECM & far-ECM) rigidity master curves. The intracellular data shown in Figure 5A are plotted here again in blue. The pericellular (near-ECM) data (which in Figure 5A is plotted in green) and extracellular (far-ECM) data are both plotted in red. In black, all of the power law fit parameters to the hysteresivity data, along with the corresponding master curve fit line, are shown.

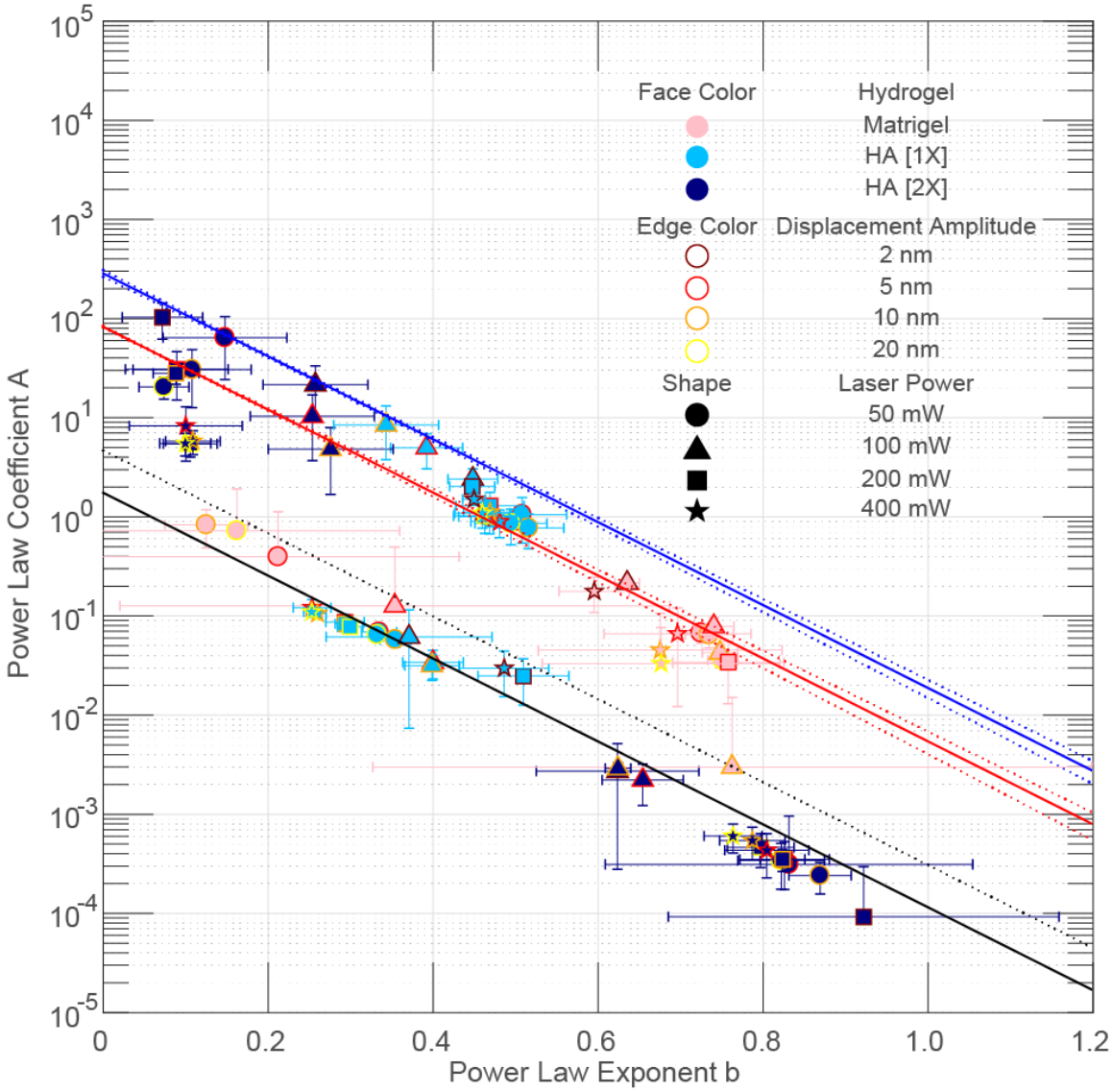

Fig. S10. Stress and strain amplitude and concentration modulation in reference gels. Test measurements were conducted on samples of Matrigel (pink markers), HA gel (light blue markers) and heavily cross-linked HA gel (dark blue markers) not seeded with cells. The active microrheology measurements were conducted at 4 different stress amplitudes corresponding to trap beam powers of 50 mW (circles), 100 mW (triangles), 200 mW (squares), and 400 mW (concave decagons) measured at the microscope backport, and at 4 different strain amplitudes of 2 nm (dark red marker edges), 5 nm (red marker edges), 10 nm (orange marker edges), and 20 nm (yellow marker edges). Blue, red and black lines reproduced from Figure 5 and Fig. S9 for reference.

Supplementary Methods

Graphical Methods

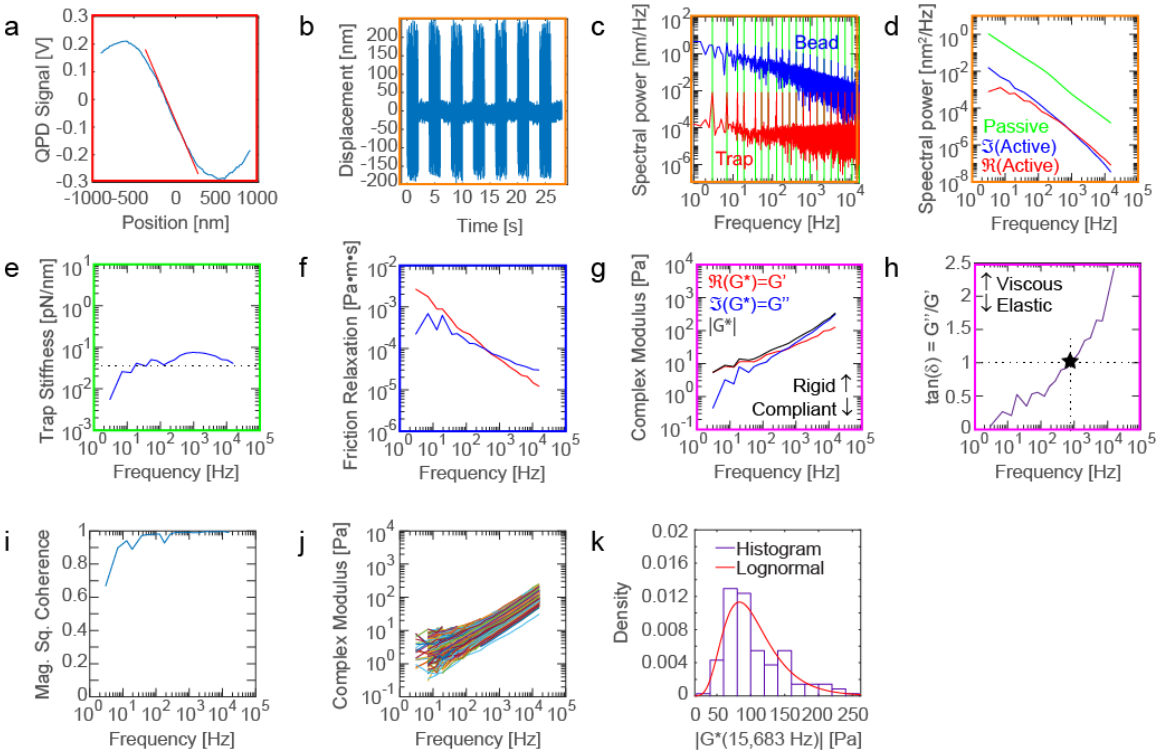

Fig. S11. Overview of methods to obtain complex moduli from optical trap based active microrheology experiments. a) Stuck-bead piezo scan with QPD signal vs. position. b) Active-passive pulse time series showing bead displacement. c) Spectra from active and passive pulses obtained by Fourier transforming the time series. Green lines indicate the 20 probe frequencies at which the trap position is simultaneously oscillated d) Real (red) and imaginary (blue) parts of the active spectrum and the passive spectrum (green) obtained from the spectral power. e) Trap stiffness given by active and passive spectra, with dashed line showing log-mean fit to high frequency values to obtain the frequency-independent trap stiffness. f) Real (red) and imaginary (blue) parts of friction relaxation spectrum. g) Real (red) and imaginary (blue) parts of the complex modulus obtained from friction relaxation spectrum. h) Loss tangent obtained from complex modulus components. i) Magnitude squared coherence $C_{xy}(\omega)=\sum_{t=-\infty}^{\infty}\left[\sum_{\tau=-\infty}^{\infty}[x(\tau)y(\tau+t)]d\tau\right]\exp(-i\omega t)dt$ of bead and trap time series. j) Plot showing all of the $|G^*(\omega)|$ *vs.* ω curves from one experimental block. k) Histogram of showing the distribution of the data at the highest frequency in the center-left plot, with a log-normal fit.

Determination of Mechanical Properties. The linear viscoelastic mechanical response of the material is modeled by a generalized Langevin equation with additional force terms (a harmonic

term accounting for the attractive potential of the optical trap and an acceleration memory term accounting for the elastic in-phase response) for undriven motion (1-4)(Eq. 1)

$$mx_U(t) = F_{random}(t) - kx_U(t) - \int_0^\infty \gamma_{1,U}(\tau)x_U(t-\tau)d\tau - \int_0^\infty \gamma_{2,U}(\tau)x_U(t-\tau)d\tau \quad (1)$$

where t is time, τ is correlation time, $x_U(t)$, $x_U(t)$, $x_U(t)$ are respectively the undriven bead position, velocity and acceleration, $F_{random}(t)$ is the Brownian force, k is the optical trap stiffness, m is the bead mass, $\gamma_{1,U}(\tau)$ and $\gamma_{2,U}(\tau)$ are respectively the real and imaginary parts of the undriven friction relaxation spectrum. The driven motion is similarly described (Eq. 2)

$$mx_D(t) = F_{random}(t) - k(x_D(t) - x_L(t)) - \int_0^\infty \gamma_{1,D}(\tau)x_D(t-\tau)d\tau - \int_0^\infty \gamma_{2,D}(\tau)x_D(t-\tau)d\tau \quad (2)$$

where $x_D(t)$, $x_D(t)$, $x_D(t)$ are respectively the driven bead position, velocity and acceleration, $x_L(t)$ is the position of the optical trap, and $\gamma_{1,D}(\tau)$ and $\gamma_{2,D}(\tau)$ are respectively the real and imaginary parts of the driven friction relaxation spectrum(Fischer & Berg-Sørensen, 2007; Berg-Sørensen & Flyvbjerg, 2004; Berg-Sørensen et al., 2006; Tolić-Nørrelykke et al., 2006). By Onsager's regression hypothesis, the fluctuation dissipation theorem identifies the undriven and driven friction relaxation spectra such that $\gamma_{1,D}(\tau) = \gamma_{1,U}(\tau)$ and $\gamma_{2,D}(\tau) = \gamma_{2,U}(\tau)$(1-4). In the frequency domain, the (complex) friction relaxation spectrum $\gamma_D(\omega)$ can thus be related by (Eq. 3)

$$\gamma_D(\omega) + i\omega m = -\frac{k}{i\omega}\left(\frac{1}{i\omega R_L(\omega)} + 1\right) \quad (3)$$

where $i^2 \equiv -1$, ω is the probe frequency of the driving oscillation in rad•s^{-1}, and $R_L(\omega)$ is the (complex) spectral power at the probe frequencies (Eq. 4)

$$R_L(\omega) \equiv \frac{x_{dr}(\omega)}{-i\omega x_L(\omega)} \tag{4}$$

where $x_L(\omega)$ and $x_{dr}(\omega)$ are the (discrete, unilateral) Fourier transforms of the time series of the positions of the trapping laser and the driven bead respectively, recorded while the trap is oscillating. The stiffness (Eq. 5) is

$$k = \frac{\Re\{R_L(\omega)\}}{P_U(\omega)} \tag{5}$$

where $\Re\{R_L(\omega)\}$ is the real part of the driven spectral power and $P_U(\omega)$ is the undriven spectral power (power spectrum) at the probe frequencies (Eq. 6)

$$P_U(\omega) \equiv \left\langle \left| x_U(\omega) \right|^2 \right\rangle \tag{6}$$

where $x_U(\omega)$ is the (discrete, unilateral) Fourier transform of the time series of the undriven bead's position while the trap is held stationary. The generalized Stokes-Einstein relation gives the (complex) shear modulus $G^*(\omega)$ as (Eq. 7)

$$G^*(\omega) = \frac{i\omega\gamma_D(\omega)}{6\pi a} \tag{7}$$

where a is the bead hydrodynamic radius.

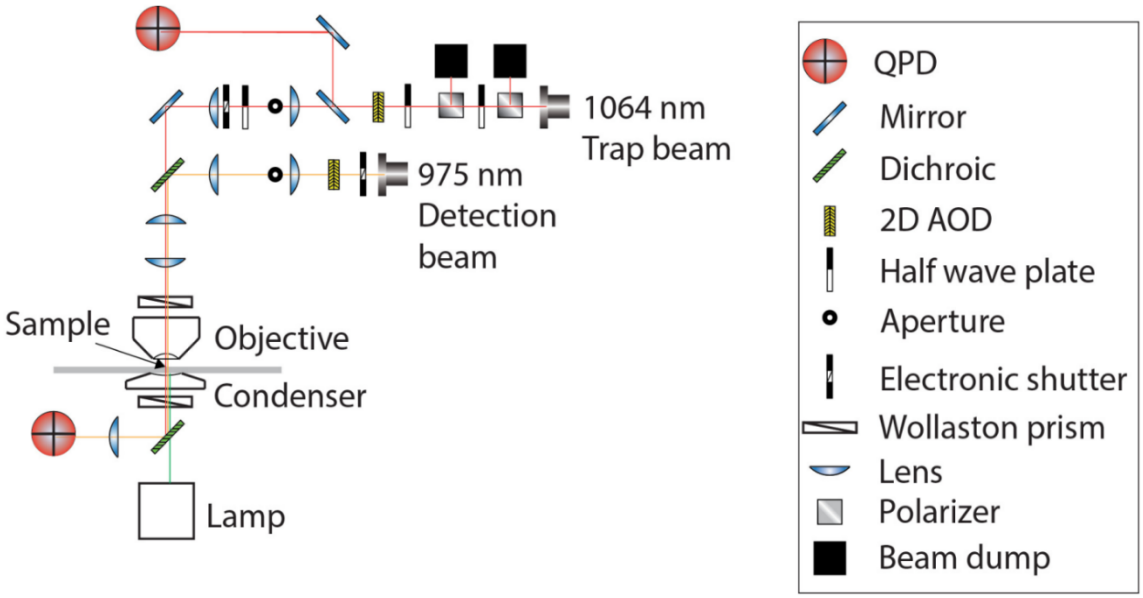

Fig. S12. Schematic of Dual beam optical tweezers

Optical Trap Instrumentation and Setup. Our instrument consists of a 1064 nm trapping beam (IPG Photonics, #YLR-20-1064-Y11) and a 975 nm detection beam (Lumics, #LU0975M00-1002F10D). The trapping beam is oscillated by a dual axis acousto-optic deflectors (AODs) (IntraAction, DTD274HD6). An iris after the AOD selects the doubly diffracted beam (*i.e.* 1st order in both transverse axes)(5-7). The AOD receives control signals from radio frequency generating cards (Analog Devices, #AD9854/PCBZ) with onboard temperature-controlled crystal oscillators (Anodyne Components, ZKG10A1N-60.000M). The cards are controlled by digital outputs from a data acquisition card (National Instruments, PCIe-5871R FPGA). AODs are mounted on 5-axis adjustable mounts (Newport, New Focus 9081). Both beams are shuttered electronically (Uniblitz, VS1452Z0R3). Polarizing beam splitter cubes (Thorlabs, PBS23) linearly polarize the trapping beam. Before entering the AOD, the beam is attenuated manually by half-wave plates (Thorlabs, WPH05M-1064) or electronically via analog output from the data acquisition card. To detect the displacement of the trapping beam's position, a beam sampler mirror (Thorlabs, BSF10-C) and neutral density (ND) filter (Thorlabs, NENIR210B) after the AOD direct a small amount of power (~1 %) onto the 'trap' quadrant photodiode (QPD) (First Sensor,

QP154-QHVSD). The trapping beam is expanded by a lens pair (Thorlabs, LA1509-C, 100 mm; AC508-200-B, 200 mm) and directed into the microscope (Nikon, Eclipse Ti-U) backport with a broadband mirror (Thorlabs, BB1-EO3IR). A lens pair (Thorlabs, LA1131-C, 50 mm; AC508-200-B, 200 mm) expands the detection beam, which is then coupled into and aligned with the trapping beam by a dichroic mirror (Chroma, T1020LPXR). A third lens pair (Thorlabs, LA113-C, 50 mm; LA1384-CA, 125 mm) expands both beams so the trapping beam slightly overfills the back aperture of the objective (Nikon, MRDO7602 CFIPLAN-APO VC60XA WI 1.2 NA). A dichroic filter cube (Chroma, ZT1064rdc-2p) sends both beams into the objective. A high numerical aperture (NA), long working distance (WD) condenser (Nikon, WI 0.9NA) collects the light from the objective. Behind the condenser, a dichroic mirror (Chroma, ZT1064RDC-2P) directs the detection beam through a relay lens that is positioned to image the back focal plane of the condenser onto the 'detection' QPD. The trapping beam is removed from the path to the QPD with a bandpass filter (Chroma, ET980/20X). Time-correlated 'trap' and 'detection' QPD signals are collected by analog inputs of the DAQ card. Control and data collection are conducted in custom programs (National Instruments, LabVIEW). A charge-coupled device (CCD) camera is mounted to the optical table. This enables position adjustments in X, Y and Z to place the camera in a plane conjugate to the trapping beam AOD, back-aperture of the condenser, and detection QPD. The Hz-nm constant relating the AOD's RF control signal (in Hz) to the beam displacement (in nm) is calibrated by attenuating and focusing the beam on a coverslip and imaging the backscattered beam on the CCD camera. Before each experiment, the alignment of the beams and the back focal plane interferometer is confirmed. Laser power is measured at the microscope backport with a power meter (Fieldmate, Coherent) and adjusted to 100 mW (or as specified) at the half-wave plate. A flow chamber is constructed from a microscope slide and cover slip with double-sided tape (Scotch) and loaded by capillary action with latex beads (Life Technologies, F13083) suspended at low concentration in water. A bead is trapped, and the trap is oscillated while simultaneously viewing the bead position in real time from the 'detection' QPD signal. The beam-coupling dichroic and the QPD position are adjusted until oscillations in both transverse axes are centered on the QPD. When

the system is aligned, a thermal power spectrum is recorded and fitted to a Lorentzian to calculate the viscosity of the water to confirm the system is calibrated. Before measurements, the camera pixel coordinates of the trap's position are found by fitting a centroid to the intensity of an image collected of a trapped, stationary bead in water.

3D centering and in situ calibration of back focal plane interferometric position detection system. With the instrument prepared as described above, a sample is placed in focus and the condenser is placed in Kohler illumination(5-7). A bead is chosen for measurement by clicking on it on the camera view display and brought to the camera pixel coordinates of the trap position using a piezo XYZ nanopositioning stage (Prior, #77011201). Then the bead is positioned precisely in the center of the trap by scanning it through the detection beam in three dimensions with the piezo stage while recording the voltages from the QPD as follows. First, it is scanned along the oscillation axis (Top-Bottom on the QPD). The characteristic V-nm plot of QPD voltage vs. position has a central linear region around which it reverses in either direction, giving local extrema at two positions corresponding to the vertical centers of the top two quadrants and bottom two quadrants of the photodiode. The stage is then moved to place the bead at the position of minimal voltage corresponding to the center of the bottom two quadrants. Next, the stage is scanned along Z, the detection beam axis. As the bead passes through the detection beam focus, the Top-Bottom voltage is further minimized, reaching another local minimum. The Z position of the piezo stage is then moved to place the bead corresponding the position of the minimum. Next, the bead is re-positioned along the Top-Bottom axis to the position between the local minimum and local maximum, i.e. the center of the linear response region that corresponds to the line separating the Top and Bottom quadrants. Then, the stage is moved in the Left-Right axis, and the bead is likewise positioned halfway between the local minimum and maximum of the Left-Right QPD signal *vs.* piezo position. Finally, the stage is scanned and re-centered along the Top-Bottom

axis again. The slope of the central linear region of the final V-nm plot gives the inverse optical sensitivity in V/nm.

in situ calibration of optical trap stiffness and active-passive microrheology. With the bead positioned in the trap as described above, the trap is oscillated while both the 'trap' and 'detection' QPD signals are recorded. The oscillation is multiplexed, *i.e.* a superposition of sine waves of differing phase and frequency, with the same amplitude at each frequency (25.4 nm per frequency or as specified). The frequencies are prime numbers to avoid interference of harmonics with fundamentals. Four phases are interlaced to minimize the total amplitude of the composite waveform. This waveform is pulsed for 2 s, followed by 2 s with the trap stationary to record the bead's passive motion. This is repeated until 7 active-passive pulse sequences are recorded.

Gel Preparation. Before experiments, cells were detached, pelleted, counted, and resuspended in 20 µL growth medium at 2×10^5 *cells/mL* in a microcentrifuge tube, to which *2 µL* of beads (1×10^{10} stock solution Life technologies, Fluospheres, F13083, Lot 1694765) was added before *30 – 60 minutes* gentle mixing on a shaker at *37°C* (Thermo-Fisher Hybaid Shake'n'Stack). Hyaluronic acid (HA) hydrogels were prepared as follows. Frozen dry stocks of thiol-modified hyaluronic acid (ESI-BIO, Glycosil) and diacrylated polyethylene glycol (ESI-BIO, Extralink Lite) were separately dissolved in degassed deionized water at $10\ mg{\bullet}mL^{-1}$, and vortexed *30 minutes*. The cell-and-bead suspension was added to *80 µL* Glycosil solution and thoroughly mixed with a micropipette, and *20 µL* Extralink Lite solution was added and thoroughly mixed again. Matrigel hydrogels were prepared as follows. Matrigel stored at *-80°C* was gradually thawed overnight (Mr. Frosty) and kept at *4°C* on ice. The cell-and-bead suspension was added to *100 µL* of chilled Matrigel solution and thoroughly mixed with a micropipette. Acid soluble highly concentrated rat tail collagen type I gels (BD Biosciences) were prepared as described previously(7). Samples were prepared by pipetting *33 µL* of prepolymerized gel solution onto a

glass microscope slide. Cover slips were attached on either side of the gel to the slide, and a third enclosing it from the top, to create a custom flow chamber using double-sided tape. The flow chambers were then incubated for *90 minutes* at *37°C*, *5 % CO2* for polymerization. Gels were then wetted with *50 μL* of drug solution and returned to the incubator for *60 minutes* at which time gels were either measured in the following *0 – 4 h* or the following day at *24 – 28 h*. Beads were phagocytosed by the cells and determined to be distributed randomly within the cell by fluorescence microscopy.

Descriptive Statistics. Samples were prepared and measured in triplicate per condition with at least 30 beads per sample measured. Because the modulus magnitudes |G*(ω)| are log-normal distributed (see Supplementary Figure 11K), we characterize their central tendency and dispersion respectively by the maximum-likelihood estimate of the log-transformed mean (Eq. 8)

$$\mu = \exp\left[\frac{1}{n}\sum_{i=1}^{n}\ln(x_i) + \frac{1}{2}\left[\frac{1}{n-1}\sum_{j=1}^{n}\left|\ln(x_j) - \frac{1}{n}\sum_{i=1}^{n}\ln(x_i)\right|^2\right]\right] \tag{8}$$

and the maximum-likelihood estimate of the log-transformed variance (Eq. 9)

$$\sigma^2 = \mu^2\left[\exp\left[\frac{1}{n-1}\sum_{j=1}^{n}\left|\ln(x_j) - \frac{1}{n}\sum_{i=1}^{n}\ln(x_i)\right|^2\right] - 1\right] \tag{9}$$

Because loss tangents tan(δ) are gaussian-distributed, we characterize their central tendency and dispersion respectively by the arithmetic mean and variance.

Effect Sizes and Multifactorial Analysis of Variance 6-way ANOVA on all tan(δ) data gives p-values and effect sizes (in terms of partial eta squared) for gel type ($p=3.84\times10^{-117}$, η_P^2

$=19.95\times10^{-2}$), cell type ($p=5.39\times10^{-43}$, $\eta_P^2=8.21\times10^{-2}$), drug treatment ($p=8.86\times10^{-11}$, $\eta_P^2=2.07\times10^{-2}$), location ($p=2.72\times10^{-81}$, $\eta_P^2=14.44\times10^{-2}$), time post embedding ($p=1.36\times10^{-20}$, $\eta_P2=3.57\times10^{-2}$) and frequency ($p<1\times10^{-200}$, $\eta_P2=65.38\times10^{-2}$). 6-way ANOVA on all |G*| data gives p-values and effect sizes for gel type ($p=2.87\times10^{-5}$, $\eta_P^2=0.73\times10^{-2}$), cell type ($p=3.08\times10^{-30}$, $\eta_P^2=5.89\times10^{-2}$), drug treatment ($p=3.32\times10^{-6}$, $\eta_P^2=1.18\times10^{-2}$), location ($p=1.92\times10^{-228}$, $\eta_P^2=35.65\times10^{-2}$), time post embedding ($p=1.77\times10^{-4}$, $\eta_P^2=0.59\times10^{-2}$) and frequency ($p=1.67\times10^{-137}$, $\eta_P^2=24.38\times10^{-2}$).

Power Law Fitting The nonlinear regressions to fit the power law and structural damping models were performed on the mean value at each frequency of tan(δ) and |G*(ω)| (computed from Eq. 8 above), from the high frequencies only (400 Hz – 15 kHz). Fits were performed in MATLAB with nonlinear least-squares regression using the Levenberg-Marquardt algorithm and robust weighting with the Least Absolute Residual procedure. The resulting fit parameters for three cell lines are plotted in Supplementary Figures 13 and 14 below.

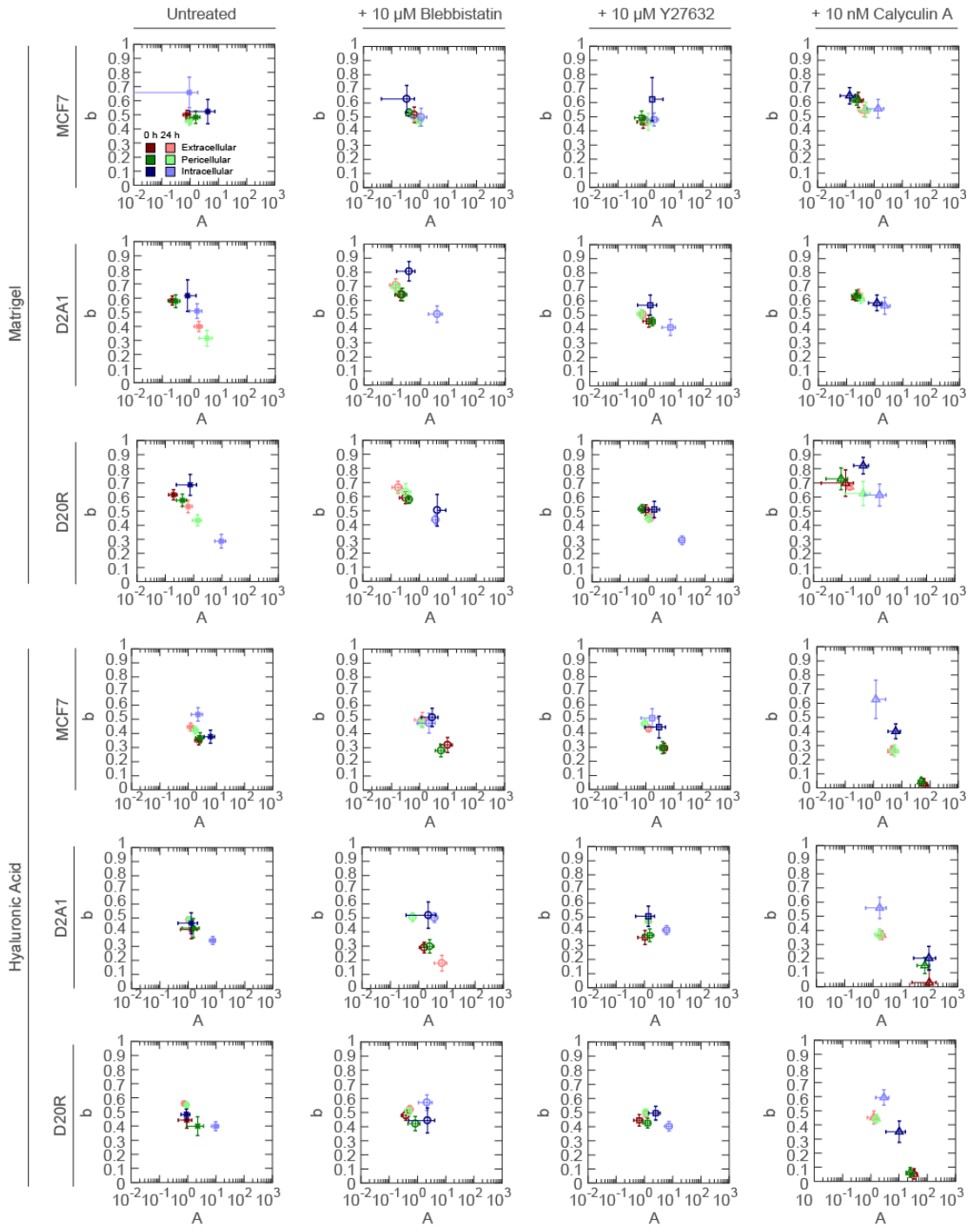

Fig. S13. Power law $|G^*| = A\omega^b$ fit coefficients plotted against fit exponents. Panel of plots of data from measurements arranged vertically by gel type and cell type, and arranged horizontally by drug type and measurement time. Fits to the power law $|G^*(\omega)| = A\omega^b$ described above yield the best fit for parameters A and b and their values at 95% confidence interval. Each plot shows the power law fit exponents b plotted against the power law fit exponents A, with vertical and horizontal error bars indicating the confidence intervals.

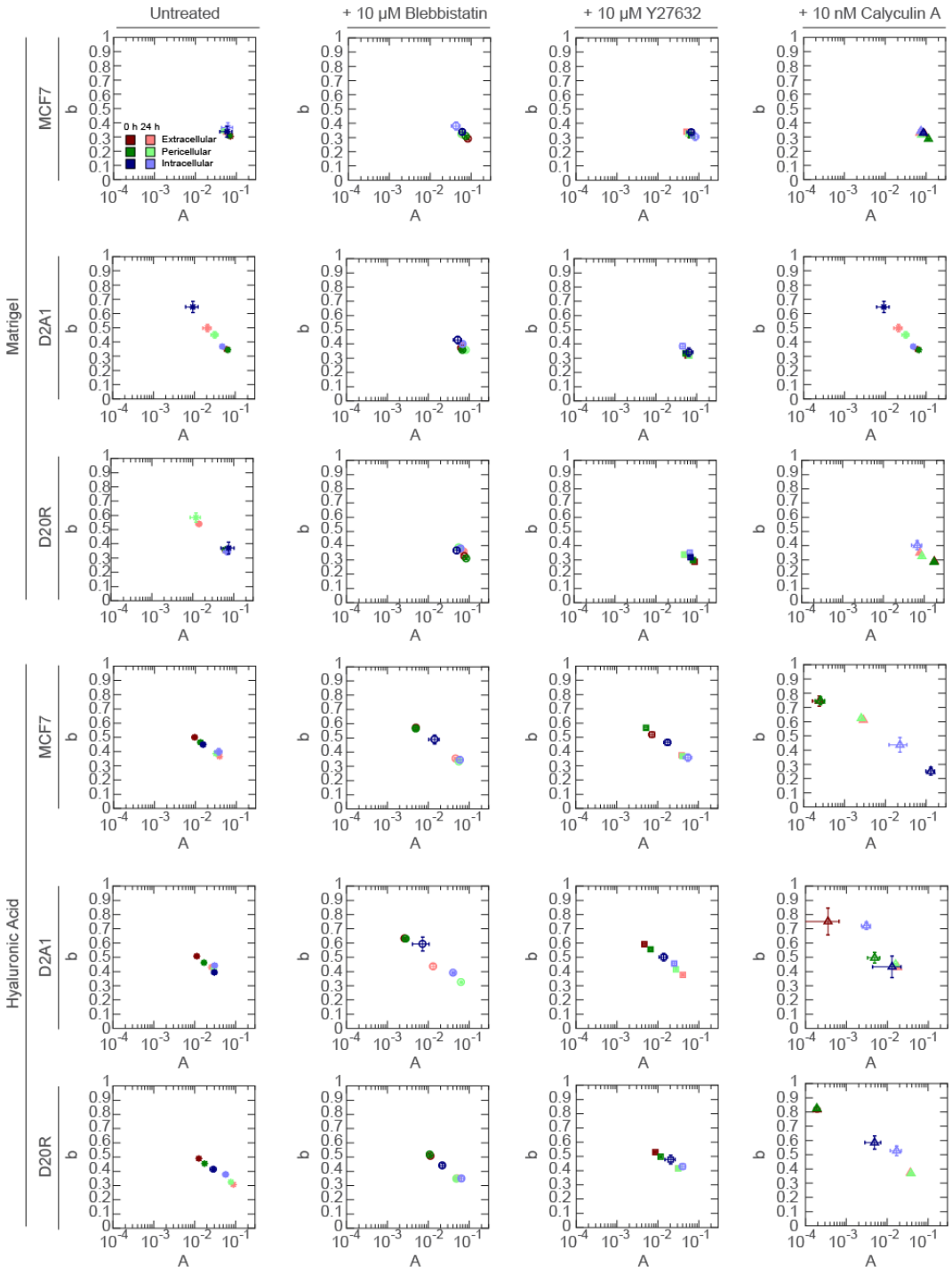

Fig. S14. Power law $\tan(\delta) = A\omega^b$ fit coefficients plotted against fit exponents. Panel of plots of data from measurements arranged vertically by gel type and cell type, and arranged horizontally by drug type and measurement time. Fits to the power law $\tan(\delta) = A\omega^b$ described above yield the best fit for parameters A and b and their values at 95% confidence interval. Each plot shows the power law fit exponents b plotted against the power law fit exponents A, with vertical and horizontal error bars indicating the confidence intervals.

Master Curve Fitting Correlation coefficients and rank correlation coefficients between the power law fit coefficient A and exponent b data are as follows. Intracellular |G*|, b *vs.* ln(A): Kendall's tau = -0.5604 (p = 9.4560e-14), Spearman's rho = -0.7454 ($p < 1\times10^{-200}$), Pearson's r = -0.8014 ($p = 1.5272\times10\text{-}^{19}$); Pericellular and Extracellular gel |G*|, b *vs.* ln(A): Kendall's tau = -0.7649 ($p = 7.0552\times10^{-48}$), Spearman's rho = -0.9168 ($p < 1\times10^{-200}$), Pearson's r = -0.9436 ($p = 1.0867\times10^{-79}$); tan(δ), b *vs.* ln(A): Kendall's tau = -0.7963 ($p = 3.2203\times10^{-77}$), Spearman's rho = -0.9352 ($p < 1\times10^{-200}$), Pearson's r = -0.9613 ($p = 1.2685\times10^{-138}$).

Initial independent fit results from nonlinear least-squares regression using the Levenberg-Marquardt algorithm and robust weighting with the Least Absolute Residual procedure to models of the form A = exp((α - b)/β) are as follows. Intracellular |G*|: α = 0.55 (0.53, 0.58), β = 0.1145 (0.1047, 0.1242), SSE = 190.1, RMSE = 1.55, Adjusted R-square = 0.98; Pericellular and Extracellular |G*|: α = 0.48 (0.47, 0.49), β = 0.1109 (0.1081, 0.1136), SSE = 141.7, RMSE = 0.94,
Adjusted R-square = 0.99; tan(δ): α = 0.05 (0.05, 0.06), β = 0.1013 (0.1002, 0.1024), SSE = 0.001582, RMSE = 0.002546, Adjusted R-square = 0.997.

Subsequent fitting results from nonlinear least-squares regression to the same model with a global fit to β, using nonlinear least squares fitting (nlinfit) using the Levenberg-Marquardt algorithm and robust weighting with the 'fair' robust weighting function (w = 1/(1 + |r|)) are as follows. β = 0.1103 (0.1013, 0.1193) and α_1 = 0.6238 (0.5930, 0.6545) for intracellular |G*|, α_2 = 0.4821 (0.4484, 0.5157) for peri- and extracellular |G*|, and α_3 = 0.0354 (0, 0.9148) for tan(δ).

Final independent fit results from nonlinear least-squares regression using the Levenberg-Marquardt algorithm and robust weighting with the Least Absolute Residual procedure to

constrained models of the form A = exp((α - b)/0.1103) are as follows. α_1 = 0.6307 (0.629, 0.6324), SSE = 24.28, RMSE = 0.5475, Adjusted R-square = 0.9977 for intracellular |G*|, α_2 = 0.4822 (0.4814, 0.483), SSE = 30.4157, RMSE = 0.4320, Adjusted R-square = 0.9983 for pericellular and extracellular |G*|, α_3 = 0.02753 (0.02714, 0.02792), SSE = 7.33971×10^{-4}, RMSE = 0.0017, Adjusted R-square = 0.9986 for tan(δ).

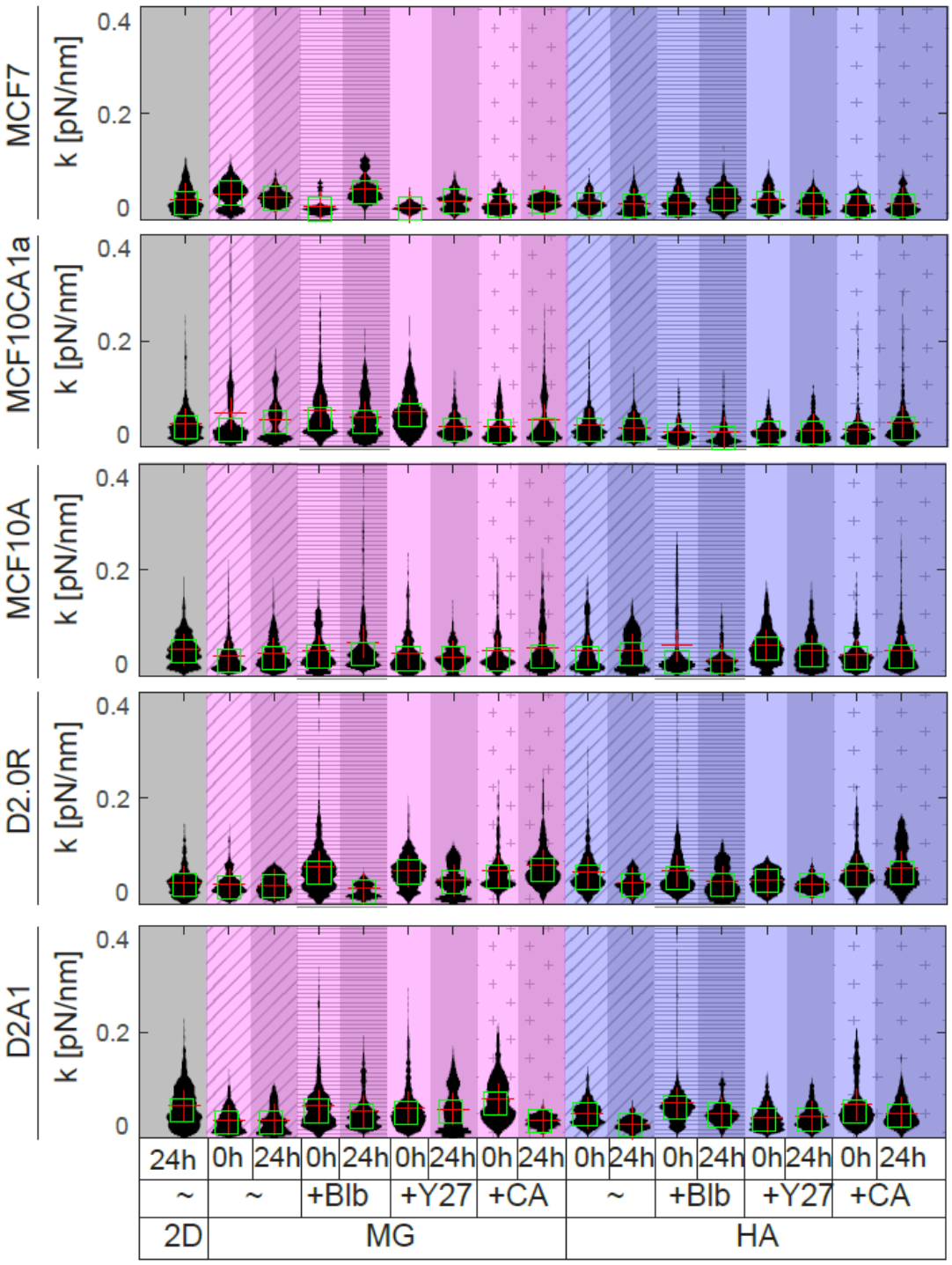

Fig. S15. Violin plots of distributions of optical trap stiffness values measured inside cells in different conditions. The trap stiffness or spring constant k varies from bead to bead due to mechanical and optical scattering heterogeneities, especially inside cells

Movie S1. Live imaging of z-axis stack shows that these 1 micron diameter beads (red) were randomly distributed in MCF7 with respect to the actin cytoskeleton and the nucleus.

Movie S2. Live imaging of untreated (control) MCF7 cells with red beads embedded in hyaluronic acid (HA) in two different time sets of 0-4 hour post-seeding and 24-28 hour post-seeding with respect to the actin cytoskeleton and the nucleus.

Movie S3. Live imaging of MCF7 cells with red beads embedded in Matrigel (lrECM) with treatment of inhibitors (Blebbistatin, Y-27632, and Calyculin A) confirming no change of bead distribution inside the cell compared to untreated (control) MCF7 cells.

1. Fischer M, Richardson AC, Reihani SN, Oddershede LB, & Berg-Sorensen K (2010) Active-passive calibration of optical tweezers in viscoelastic media. *Rev Sci Instrum* 81(1):015103.
2. Berg-Sørensen K & Flyvbjerg H (2004) Power spectrum analysis for optical tweezers. *Review of Scientific Instruments* 75(3):594-612.
3. Berg-Sørensen K, Peterman EJG, Weber T, Schmidt CF, & Flyvbjerg H (2006) Power spectrum analysis for optical tweezers. II: Laser wavelength dependence of parasitic filtering, and how to achieve high bandwidth. *Review of Scientific Instruments* 77(6):063106.
4. Tolić-Nørrelykke SF*, et al.* (2006) Calibration of optical tweezers with positional detection in the back focal plane. *Review of Scientific Instruments* 77(10):103101.
5. Blehm BH, Devine A, Staunton JR, & Tanner K (2016) In vivo tissue has non-linear rheological behavior distinct from 3D biomimetic hydrogels, as determined by AMOTIV microscopy. *Biomaterials* 83:66-78.
6. Staunton JR, Blehm B, Devine A, & Tanner K (2017) In situ calibration of position detection in an optical trap for active microrheology in viscous materials. *Opt Express* 25(3):1746-1761.
7. Staunton JR*, et al.* (2016) Mechanical properties of the tumor stromal microenvironment probed in vitro and ex vivo by in situ-calibrated optical trap-based active microrheology. *Cell Mol Bioeng* 9(3):398-417.